Available online at www.sciencedirect.com
ScienceDirect
Trans. Nonferrous Met. Soc. China 35(2025) 1975−1986
Transactions of Nonferrous Metals Society of China
www.tnmsc.cn

Crystal growth kinetics of single-crystal Ni-rich layered cathodes for high-energy lithium-ion batteries

Feng LI[1#], Yu-hang TIAN[1#], Lu-xia GE[1], Sheng-long FAN[1], Mao-sheng GONG[1], Ke FAN[2], Pei-yu HOU[1], Xian-qi WEI[1]

1. School of Physics and Technology, University of Jinan, Jinan 250022, China;
2. Research Institute of Smart Energy, Department of Applied Physics, The Hong Kong Polytechnic University, Hong Kong 999077, China

Received 26 September 2023; accepted 13 May 2024

Abstract: The effects of synthesis conditions, especially the heating rate, on the reaction kinetics of Ni-rich cathodes were systematically studied. The growth rate of Ni-rich oxide increases continuously as the heating rate increases. Ab initio molecular dynamics simulations demonstrate that a high heating rate induces anabatic oscillations, indicating a decrease in thermodynamic stability and a tendency for the crystal surface to undergo reconstruction. The presence of an intermediate phase at the grain boundary amplifies atomic migration-induced interface fusion and consequently augments crystal growth kinetics. However, the excessively high heating rate aggravates the Li^+/Ni^{2+} mixing in the Ni-rich cathode. The single-crystal Ni-rich cathode exhibits enhanced structural/thermal stability but a decreased specific capacity and rate performance compared with its polycrystalline counterpart.

Key words: lithium-ion battery; Ni-rich cathode; single crystal; growth kinetics; heating rate

1 Introduction

With the development of portable electronics and electric vehicles (EVs), the demand for lithium-ion batteries (LIBs) with high energy density is becoming increasingly urgent [1]. Cathode materials, a significant component of LIBs, hold a crucial role in both their performance and cost [2,3]. The consistent pursuit objective in the past decades has been the development of high-capacity cathodes characterized by high voltage and low cost. Recently, the layered Ni-rich cathode material $LiNi_xMn_yCo_zO_2$ ($x+y+z=1$, $x\geq0.8$) has shown to deliver large specific capacities above 200 mA·h/g and high voltages up to 3.8 V when improving the upper cutoff voltage and/or Ni content and to show great potential for developing 300 W·h/kg LIBs [4−6].

The H2−H3 phase transition of Ni-rich layered cathodes causes anisotropic variations in the grains and further results in microstructural stress at the grain boundaries. Continuous accumulation of micro-stress results in the separation of primary grains and ultimately generates microcracks within polycrystalline particles [7,8]. Once microcracks occur in Ni-rich polycrystalline materials, the electrolyte immediately infiltrates the interior of the particles through the crack network, which further accelerates side reactions, structural degeneration and performance decline [9,10]. Single-crystal Ni-rich cathodes with the advantages of monodispersity

#Feng LI and Yu-hang TIAN contributed equally to this work
Corresponding author: Pei-yu HOU, Tel: +86-531-82767213, E-mail: sps_houpy@ujn.edu.cn;
Ke FAN, Tel: +852-27665694, E-mail: 18074234r@connect.polyu.hk
https://doi.org/10.1016/S1003-6326(25)66794-X

and the absence of intergrain boundaries show promise for avoiding microcracks [11,12]. Single-crystal cathodes with low specific surfaces and high mechanical strength enable good structural stability. It has been confirmed that converting polycrystalline materials into single crystals is an effective strategy for addressing microcrack problems [13−16]. Nonetheless, a significant challenge in the preparation of single-crystal Ni-rich cathodes lies in the enhancement of their crystal growth kinetics while preserving their layered characteristics and electrochemical performance [17,18].

The Arrhenius equation indicates that the sintering temperature increase can substantially enhance crystal growth kinetics [14]. Nevertheless, high temperatures easily cause phase segregation of the rock-salt structure and aggravate Li^+/Ni^{2+} mixing [13,19,20]. The proposed strategy of creating a liquid reaction medium by introducing additional lithium sources and molten salt enhances crystal growth kinetics and is widely employed for the production of single-crystal ternary cathodes. LI et al [21] discovered that the surplus lithium salt accelerated grain growth, resulting in the successful preparation of a single-crystal $LiNi_{0.5}Co_{0.2}Mn_{0.3}O_2$ cathode with a grain size of 2−4 μm. QIU et al [22] demonstrated that small precursor size (<6 μm), large Li/TM ratio (>1.0), and high temperature (≥810 °C) promote the crystal growth of the intermediate phase due to enhanced reaction kinetics. Recent studies [22−25] have established the crucial influence of precursor size, Li/TM ratio, and solid-state reaction temperature on the crystal growth of single-crystal Ni-rich cathodes. However, the heating rate, another important parameter, has long been overlooked, and its role in the crystal growth kinetics of Ni-rich cathodes remains poorly understood.

In this study, the impact of the heating rate on the crystal growth kinetics of Ni-rich cathodes during solid-state reactions was investigated. The crystal growth rate and grain size of the Ni-rich oxides increase continuously as the heating rate increases from 2 to 8 °C/min. However, the high heating rate of 8 °C/min aggravates the Li^+/Ni^{2+} mixing and increases the Li^+ diffusion barrier. As a result, a medium heating rate of 5 °C/min proves to be advantageous for the production of single-crystal Ni-rich layered cathodes. Ab initio molecular dynamics simulations indicate that the high heating rate induces anabatic oscillations around the equilibrium value, suggesting a decrease in thermodynamic stability and a tendency for the crystal surface to undergo reconstruction. The presence of an intermediate phase at the grain boundary amplifies atomic migration-induced interface fusion and consequently augments crystal growth kinetics. These findings highlight the critical role of the long-neglected heating rate in enhancing the crystal growth kinetics of single-crystal Ni-rich cathodes.

2 Experimental

2.1 Synthesis of Ni-rich cathode

The $Ni_{0.8}Co_{0.1}Mn_{0.1}(OH)_2$ precursors were synthesized by a coprecipitation route. Stoichiometric $NiSO_4·6H_2O$ (AR, 1051.4 g), $CoSO_4·7H_2O$ (AR, 140.6 g), and $MnSO_4·H_2O$ (AR, 84.5 g) (molar ratio of Ni/Co/Mn=8∶1∶1) were added to DI water under continuous stirring, and a 2.5 mol/L aqueous solution was obtained (2 L). The solution was introduced into the continuous-stirred tank reactor (CSTR) at a flow rate of 100 mL/h, and the pH level was maintained by the addition of an alkali solution comprising NaOH and ammonia. After approximately 20 h, the solution was completely consumed, and the desired precursor $[Ni_{0.8}Co_{0.1}Mn_{0.1}](OH)_2$ was prepared. In this study, a relatively low pH of 11.4 and a high concentration of ammonia complexing agent (3 mol/L) were utilized to produce target precursors with a large particle size (P1). Conversely, a relatively high pH of 12.0 and a low concentration of ammonia complexing agent (1 mol/L) were employed to prepare target precursors with a small particle size (P2). The investigation focused on examining the influence of precursor size, heating rate, molar ratio of Li/TM, and sintering temperature on the kinetics of crystal growth and the dispersion of grains in Ni-rich $LiNi_{0.8}Co_{0.1}Mn_{0.1}O_2$. Table 1 summarizes the synthesis conditions for preparing SC-NCM811 in this study. The precursors with varying particle sizes, lithium/transition metal molar ratios (Li/TM= 1.0, 1.05, and 1.1), calcination temperatures (820, 835, and 850 °C), and heating rates (2, 5, and 8 °C/min) were selected. Unless otherwise specified, the samples were annealed for 15 h and naturally cooled to room temperature in an O_2 atmosphere. The precursors $Ni_{0.8}Co_{0.1}Mn_{0.1}(OH)_2$ (P1) were

combined with stoichiometric $LiOH·H_2O$ (Li/TM= 1.0) and calcined at 800 °C to produce poly-crystalline $LiNi_{0.8}Co_{0.1}Mn_{0.1}O_2$ (PC-NCM811).

Table 1 Synthesis conditions for preparing single-crystal $LiNi_{0.8}Co_{0.1}Mn_{0.1}O_2$

Sample	Precursor	Heating rate/ (°C·min^{-1})	Li/TM molar ratio	Heating temperature/ °C
SC-1	P1	5	1.10	850
SC-2	P2	5	1.10	850
SC-3	P2	2	1.10	850
SC-4	P2	8	1.10	850
SC-5	P2	5	1.00	850
SC-6	P2	5	1.05	850
SC-7	P2	5	1.05	820
SC-8	P2	5	1.05	835

2.2 Material characterization

The phase structure of the as-prepared Ni-rich cathode materials was analyzed using X-ray diffraction (Rigaku, Cu K_α, λ=0.15406 nm). The morphologies of the precursors and cathodes were evaluated by scanning electron microscopy (SEM; Zeiss Sigma 300). The particle size and distribution of both precursors were assessed using a Mastersizer 2000 analyzer. The molar ratio of Ni/Co/Mn in both precursors was determined through inductively coupled plasma optical emission spectrometry (ICP-OES) using an iCAP 7400 instrument by Thermo. For the differential scanning calorimetry (DSC) analysis, both Ni-rich electrodes were charged to 4.3 V in half cells. Subsequently, the fully charged cells were promptly disassembled in an Ar-filled glovebox. Meanwhile, the active materials were scraped onto Al foil and placed inside a high-pressure crucible. Finally, DSC analysis was conducted using a TA Q2000 instrument over a temperature range of 150−300 °C.

2.3 Computational method

Ab initio molecular dynamics (AIMD) simulations were conducted to confirm the thermal stability of a 2 × 2 supercell of NCM811. These simulations employed the Nosé–Hoover thermostat and operated within the NVT ensemble, covering a temperature range of 450−800 K with a time step of 2 fs. All theoretical calculations were executed using the VASP code.

2.4 Electrochemical measurement

The preparation process of the electrode closely followed our previous study [11]. The active material mass loading for these working electrodes was approximately 8.0 mg/cm^2. Electrochemical evaluations of both Ni-rich cathodes were performed using 2032-type coin cells. Li foil with a diameter of 14 mm served as the counter electrode in half cells. The electrolyte consisted of 1 mol/L $LiPF_6$ dissolved in a mixed solvent blend (EC:DC:EMC=1:1:1 with 1 wt.% VC). In terms of half cells, the electrolyte dosage was 10 μL/mg. Electrochemical testing was carried out using a LAND instrument (CT−2001A, Wuhan Land) within the potential range of 2.7−4.3 V and 2.7−4.5 V (vs Li/Li$^+$). The galvanostatic intermittent titration technique (GITT) was performed at a constant rate of 0.3C (1C=200 mA/g) for 600 s and relaxed for 3600 s until the quasi-equilibrium potential was reached. The performance testing was performed at 25 and 50 °C.

3 Results and discussion

3.1 Role of precursor size in crystal growth

Normally, coprecipitation reactions involve the generation of complex $[TM(NH_3)_n]^{2+}$, nucleation of grains, and particle growth [26,27]. A high pH and low concentration of complexing agent increase the free concentration of TM^{2+} ions in the CSTR, during which the nucleation of grains dominates the coprecipitation reactions, and further precursors with small particle sizes are generated. In contrast, the relatively low pH and high concentration of the complexing agent decrease the free concentration of TM^{2+} ions in the CSTR, in which particle growth dominates during the coprecipitation reactions; therefore, the desired precursors with large particle sizes are generated. We first studied the effect of precursor particle size on the crystal growth rate of SC-NCM811. The SEM images in Figs. 1(a, b) show that both precursors exhibit well-dispersed near-spherical particles self-organized by nanosized plate-like primary grains. The particle size distributions of both precursors are depicted in Fig. 1(c). Both P1 and P2 curves exhibit a characteristic Gaussian profile, with average particle sizes (D_{50}) of 9.8 μm for P1 and 3.7 μm for P2. The XRD patterns of both precursors are shown in Fig. 1(d), in which the diffraction peaks

corresponding to the (001), (100), (101), (102), and (110) crystal planes are attributed to the hexagonal β-Ni(OH)$_2$ phase with a space group of $P\bar{3}m1$ [28]. ICP-OES analysis reveals cationic molar ratios of Ni/Co/Mn to be 0.793/0.103/0.104 for P1 precursors and 0.797/0.101/0.102 for P2 precursors, which closely match the chemical formula of $Ni_{0.8}Co_{0.1}Mn_{0.1}(OH)_2$.

The precursors of P1 and P2, mixed with stoichiometric lithium sources (Li/TM molar ratio= 1.05), were calcined at 850 °C to produce SC-1 and SC-2 samples, respectively. Figure 2(a) shows the

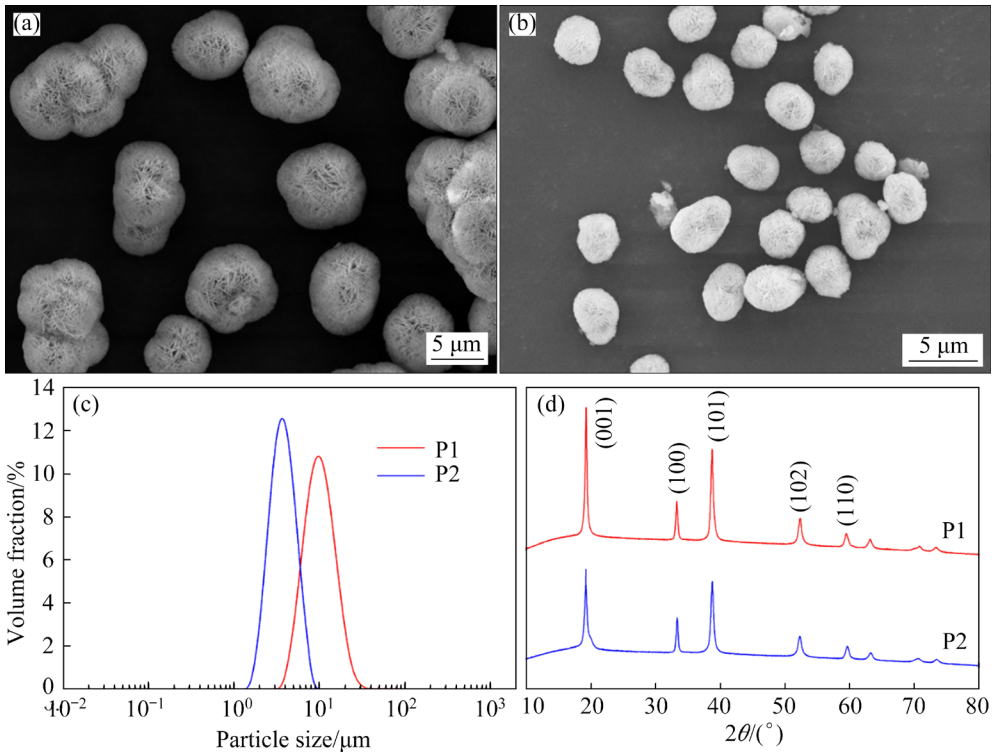

Fig. 1 SEM images of precursors (P1) (a) and (P2) (b), and particle size distribution (c) and XRD patterns (d) of both hydroxide precursors

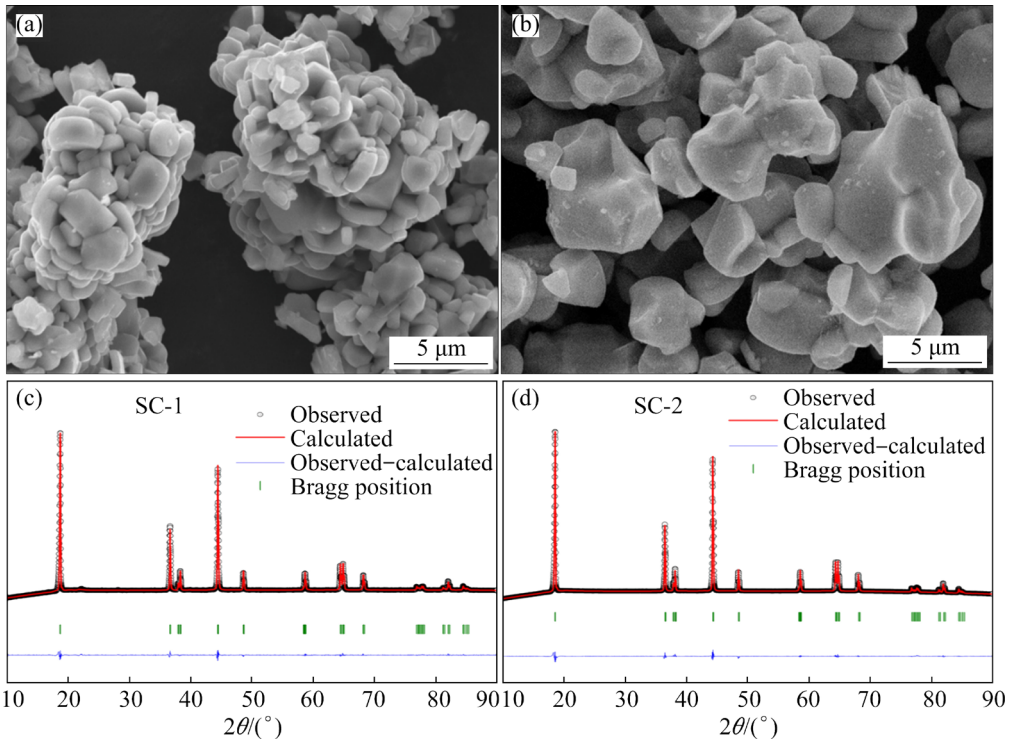

Fig. 2 SEM images (a, b) and XRD patterns (c, d) of single-crystal $LiNi_{0.8}Co_{0.1}Mn_{0.1}O_2$: (a, c) SC-1; (b, d) SC-2

obvious agglomeration of primary grains with a particle size of 1−3 μm for the SC-1 sample. The SEM image of SC-2 shows a greatly improved dispersity of irregular polyhedral grains, with grain sizes ranging from 1 to 4 μm, as shown in Fig. 2(b). A precursor with a large particle size probably has lower driving forces for grain boundary reconstruction than that with a small particle size at the same solid-state temperature. Therefore, the large particles exhibit weak grain fusion and, thereby, severe agglomeration. XRD patterns and Rietveld refinement of SC-1 and SC-2 are depicted in Figs. 2(c, d). These diffraction peaks correspond to the hexagonal α-$NaFeO_2$ layered structure [29]. Rietveld analysis reveals lattice parameters of a=2.8723 Å and c=14.1909 Å for SC-1, and a=2.8725 Å and c=14.1916 Å for SC-2. SC-1 and SC-2 exhibit Li^+/Ni^{2+} cation mixing of 3.47% and 3.18%, respectively, as detailed in Tables S1 and S2 of Supporting Information (SI). These findings affirm that precursors with smaller particle sizes are advantageous for the preparation of single-crystal cathodes characterized by superior dispersity and reduced Li^+/Ni^{2+} mixing.

3.2 Role of heating rate in crystal growth

The influence of the heating rate on the morphology and structure of Ni-rich oxides was investigated. SEM images in Figs. 3(a, c, e) reveal that the particle size and dispersity of the synthesized single crystals are strongly affected by the heating rate. At a heating rate of 2 °C/min, the

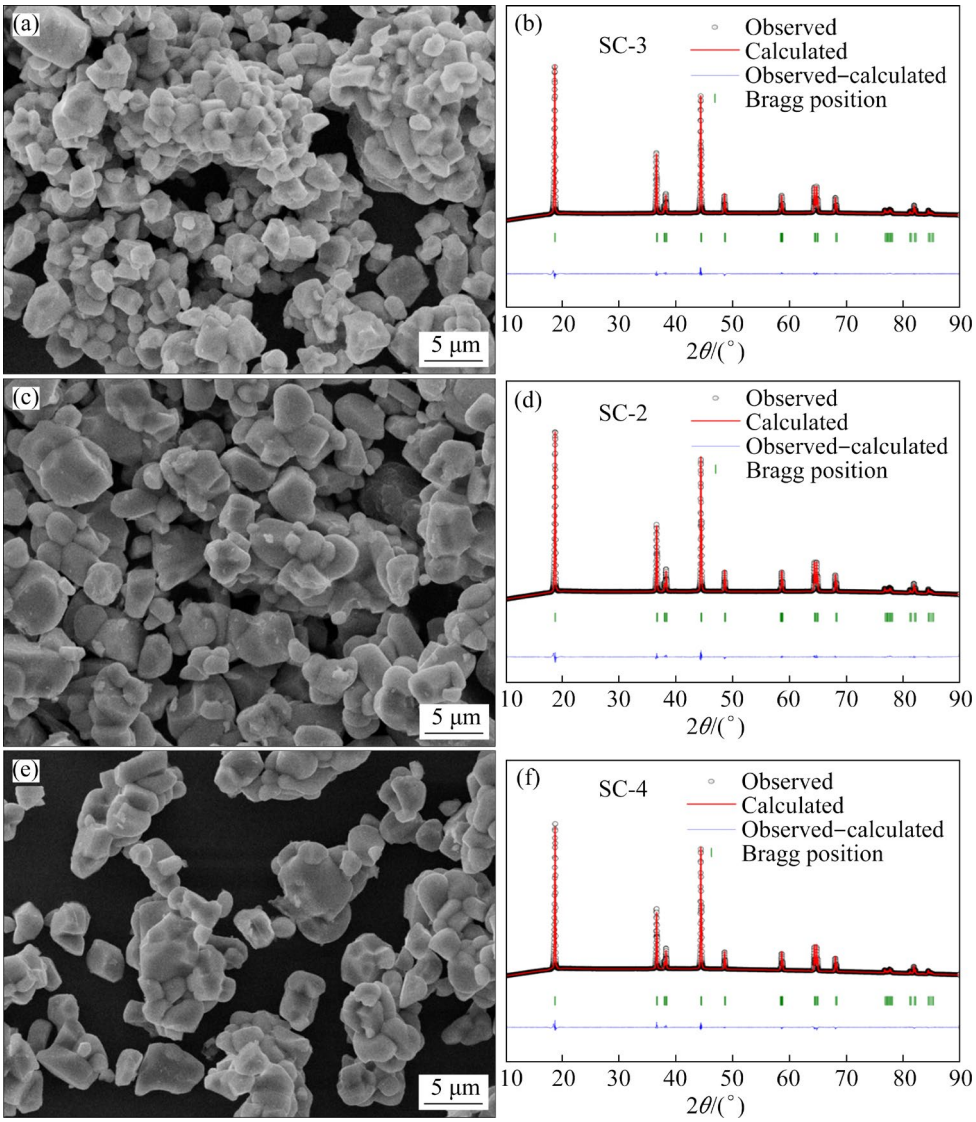

Fig. 3 SEM images (a, c, e) and XRD patterns (b, d, f) of single-crystal $LiNi_{0.8}Co_{0.1}Mn_{0.1}O_2$: (a, b) SC-3 calcined at heating rate of 2 °C/min; (c, d) SC-2 calcined at heating rate of 5 °C/min; (e, f) SC-4 calcined at heating rate of 8 °C/min

SC-3 sample displays evident grain agglomeration with a particle size ranging in 1−3 μm. As the heating rate increases to 5 °C/min, the grains in SC-2 exhibit improved dispersity with a large particle size of 2−4 μm. Continuously increasing the heating rate to 8 °C/min results in the continuous growth of grains in SC-4, reaching sizes as high as 3−5 μm. XRD patterns of Figs. 3(b, d, f) indicate that SC-2, SC-3 and SC-4 samples possess a hexagonal α-$NaFeO_2$ layered structure. The calculated lattice parameters are as follows: a= 2.88725 Å and c=14.21916 Å for SC-2, a=2.8724 Å and c=14.1919 Å for SC-3, and a=2.8726 Å and c= 14.1907 Å for SC-4, as detailed in Tables S2−S4 of SI. SC-2, SC-3 and SC-4 have Li^+/Ni^{2+} cation mixing fractions of 3.18%, 3.07% and 3.95%, respectively. As a result, the crystal growth rate and grain size of the single-crystal Ni-rich oxides increase continuously as the heating rate increases from 2 to 8 °C/min. However, the high heating rate of 8 °C/min aggravates the Li^+/Ni^{2+} mixing. In conclusion, the heating rate of 5 °C/min is deemed to be more advantageous for the production of single-crystal Ni-rich cathodes characterized by low Li^+/Ni^{2+} mixing.

It is demonstrated that thermodynamics drives interface cationic diffusion through the intermediate phase to achieve grain boundary fusion [21]. The thermal stability of NCM811 under varying heating rates was examined through ab initio molecular dynamics (AMID) simulations, as illustrated in Fig. 4. After 5 ps, both the total energy and temperature of the system display increasing oscillations around their equilibrium values. This suggests that as the temperature or heating rate rises, the thermodynamic stability of the hexagonal α-$NaFeO_2$ layered structure decreases, leading to a tendency for the crystal surface to undergo reconstruction. In other words, a high heating rate promotes the formation of the cation mixing phase at the grain boundary due to enhanced reaction kinetics. The growth of the intermediate state further intensifies atomic migration-induced interface fusion.

3.3 Role of Li/TM molar ratio and calcination temperature in crystal growth

We further investigated the impact of Li/TM molar ratios on the crystal characteristics of single-crystal Ni-rich oxides. The particle size and dispersity of the single crystals are affected by the molar ratios of Li/TM, as shown in Figs. S1(a, c, e)

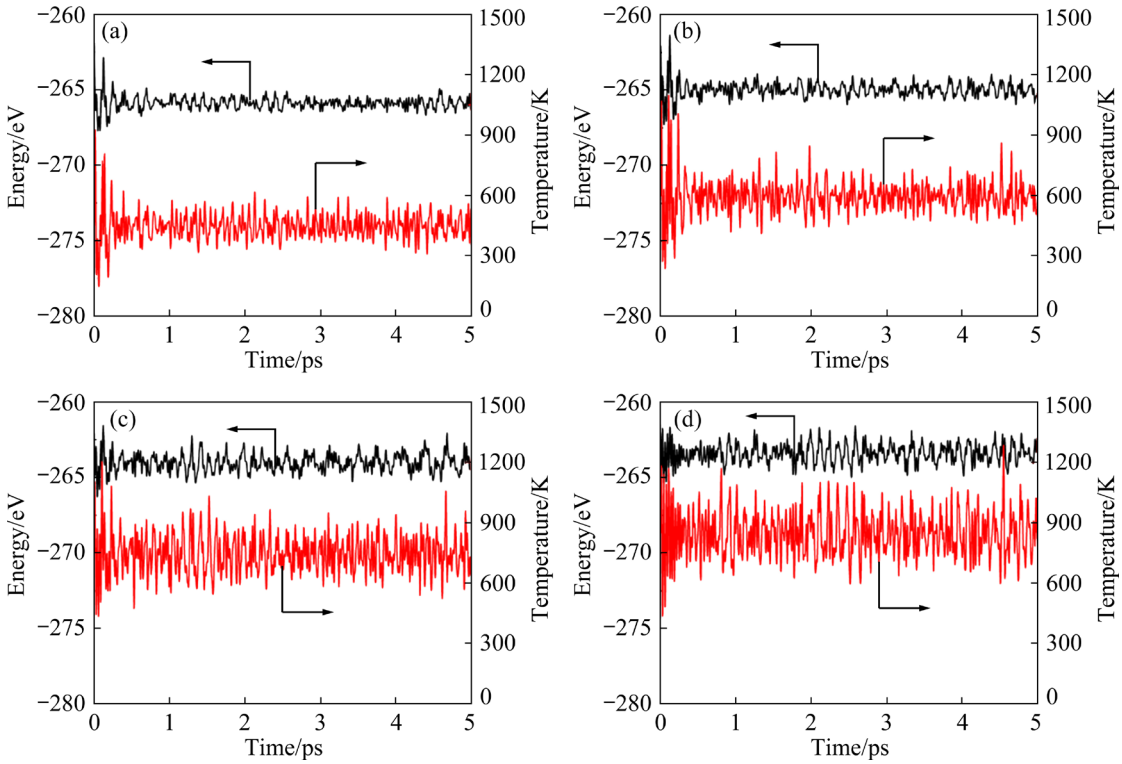

Fig. 4 Total energy and simulation temperature as functions of time for NCM811 calcined at 450 K (a), 600 K (b), 750 K (c), and 800 K (d) during AIMD simulation

of SI. At a low Li/TM molar ratio of 1.0, the SC-5 sample exhibits noticeable grain agglomeration. As the molar ratio of Li/TM increases from 1.05 to 1.1, both grain size and dispersity increase. The reaction rate (v) is described by the equation of $v=kc^{\alpha}_{\mathrm{LiOH}}c^{\beta}_{\mathrm{Ni_{0.8}Co_{0.1}Mn_{0.1}(OH)_2}}c^{\gamma}_{\mathrm{O_2}}$, where c represents the reactant concentration, k is a constant, and α, β and γ are exponents. A high concentration of LiOH (c_{LiOH}) increases the chemical reaction rate and promotes grain fusion [22]. Additionally, the additional Li sources act as a liquid molten salt (cosolvent) reaction medium, further facilitating mass and heat transfer [11,23]. XRD patterns in Figs. S1(b, d, f) of SI indicate that SC-2, SC-5 and SC-6 samples possess a hexagonal α-$NaFeO_2$ structure. The calculated lattice parameters are as follows: a=2.8725 Å and c=14.1916 Å for SC-2, a=2.8716 Å and c=14.1928 Å for SC-5, and a=2.8730 Å and c=14.1921 Å for SC-6, as detailed in Table S2, S5, and S6 of SI. SC-2, SC-5, and SC-6 exhibit Li^+/Ni^{2+} cation mixing fractions of 3.18%, 3.63%, and 3.26%, respectively.

The effect of the calcination temperature on the crystal features of single-crystal Ni-rich oxides was investigated. The SEM images in Figs. S2(a, c, e) of SI show that the particle size and dispersity of the single crystals are influenced by the calcination temperature. The SC-7 sample calcined at 820 °C exhibited obvious agglomeration of grains with a particle size of 1−2 μm. The grains of SC-8 showed an improved dispersity with a particle size of 1−3 μm when the calcination temperature was increased to 835 °C. When the calcination temperature is increased to 850 °C, the grain size and dispersity further improved. The Arrhenius equation indicates that an increase in the solid-reaction temperature leads to a higher concentration of activated molecules; thus, enhancing reaction kinetics. This suggests that the reaction rate improves with increasing temperature. XRD patterns in Figs. S2(b, d, f) of SI reveal that SC-6, SC-7, and SC-8 samples exhibit a hexagonal α-$NaFeO_2$ structure. The calculated lattice parameters are as follows: a=2.8730 Å and c=14.1921 Å for SC-6, a=2.8715 Å and c=14.1921 Å for SC-7, and a=2.8712 Å and c=14.1921 Å for SC-8, as shown in Tables S6−S8 of SI. SC-6, SC-7 and SC-8 have Li^+/Ni^{2+} cation mixing fraction of 3.26%, 2.93% and 3.01%, respectively.

In summary, small particle size precursors are advantageous for producing monodispersed single-crystal particles. Crystal growth kinetics improve significantly with increasing heating rate, Li/TM molar ratio, and sintering temperature. However, higher sintering temperatures and heating rates exacerbate Li/Ni cation mixing, while a higher molar ratio of Li/TM increases material costs. Therefore, the optimal conditions for preparing micron-sized single-crystal Ni-rich ternary $LiNi_{0.8}Co_{0.1}Mn_{0.1}O_2$ involve small particle size precursors, a Li/TM molar ratio of 1.05, a heating rate of 5 °C/min, and a calcination temperature of 835 °C.

3.4 Electrochemical performance of SC- and PC-NCM811

SEM and XRD analyses of PC-NCM811 and SC-NCM811 are presented in Fig. 5. Figure 5(a) reveals spherical secondary particles with a size ranging from 5 to 15 μm for PC-NCM811. In contrast, after wet ball-milling, Fig. 5(b) shows SC-NCM811 with monodispersed grains of approximately 2 μm in size. XRD and Rietveld refinements of both NCM811 cathodes are displayed in Figs. 5(c, d). These results confirm that both oxides possess a hexagonal α-$NaFeO_2$-type layered structure. The calculated lattice parameters obtained through Rietveld refinement are provided in Tables S9 and S10 of SI. Specifically, the lattice parameters are a=2.8726 Å and c=14.1923 Å for SC-NCM811 and a=2.8732 Å and c=14.1924 Å for PC-NCM811. SC-NCM811 and PC-NCM811 exhibit Li^+/Ni^{2+} cation mixing of 3.11% and 2.91%, respectively. Further analysis with TEM−SAED is employed to determine the single-crystal/polycrystalline nature of Ni-rich oxides, as shown in Fig. S3 of SI. The SAED result for PC-NCM811 displays a series of concentric rings with different radii, confirming its polycrystalline nature. Conversely, the SAED result for SC-NCM811 exhibits numerous perfectly arranged bright spots, demonstrating its single-crystal nature.

SC-NCM811 delivers improved cycling stability but a slightly lower reversible capacity and initial coulombic efficiency than its polycrystalline counterpart, as shown in Fig. 6. It is noted that the polycrystalline Ni-rich cathode assembled from many nanosized primary grains has a much shorter migration path of Li^+ and electrons than a micro-sized single-crystal cathode. The polycrystalline Ni-rich cathode exhibits better redox reversibility, along with higher discharged capacity and initial

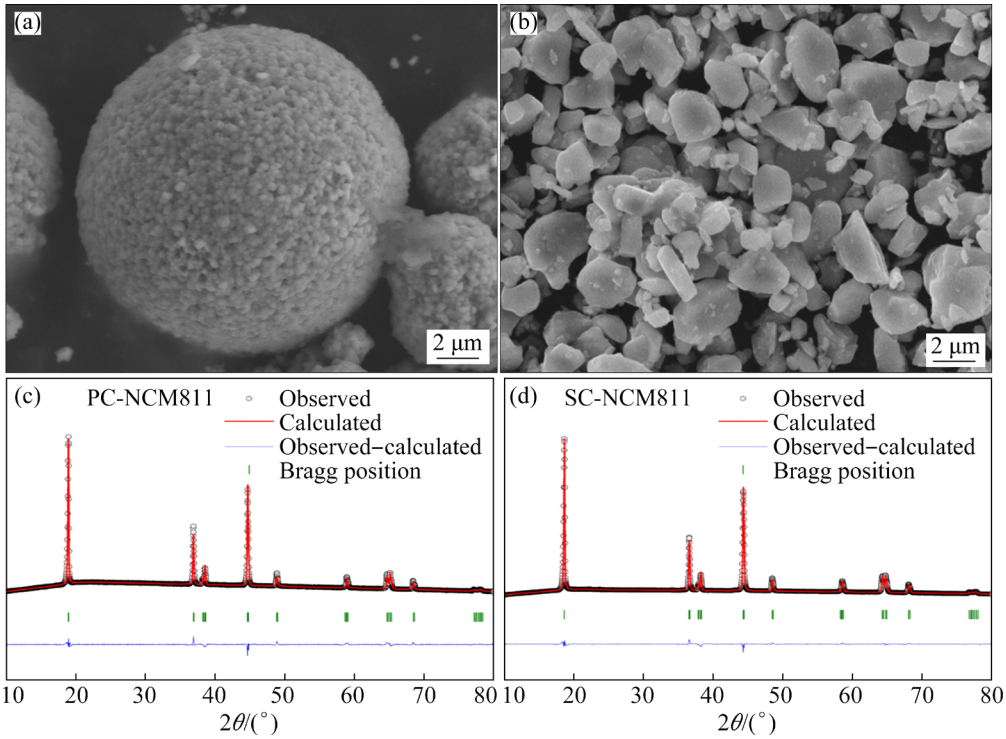

Fig. 5 SEM images (a, b) and XRD patterns and Rietveld refinement (c, d) of PC-NCM811 (a, c) and SC-NCM811 (b, d)

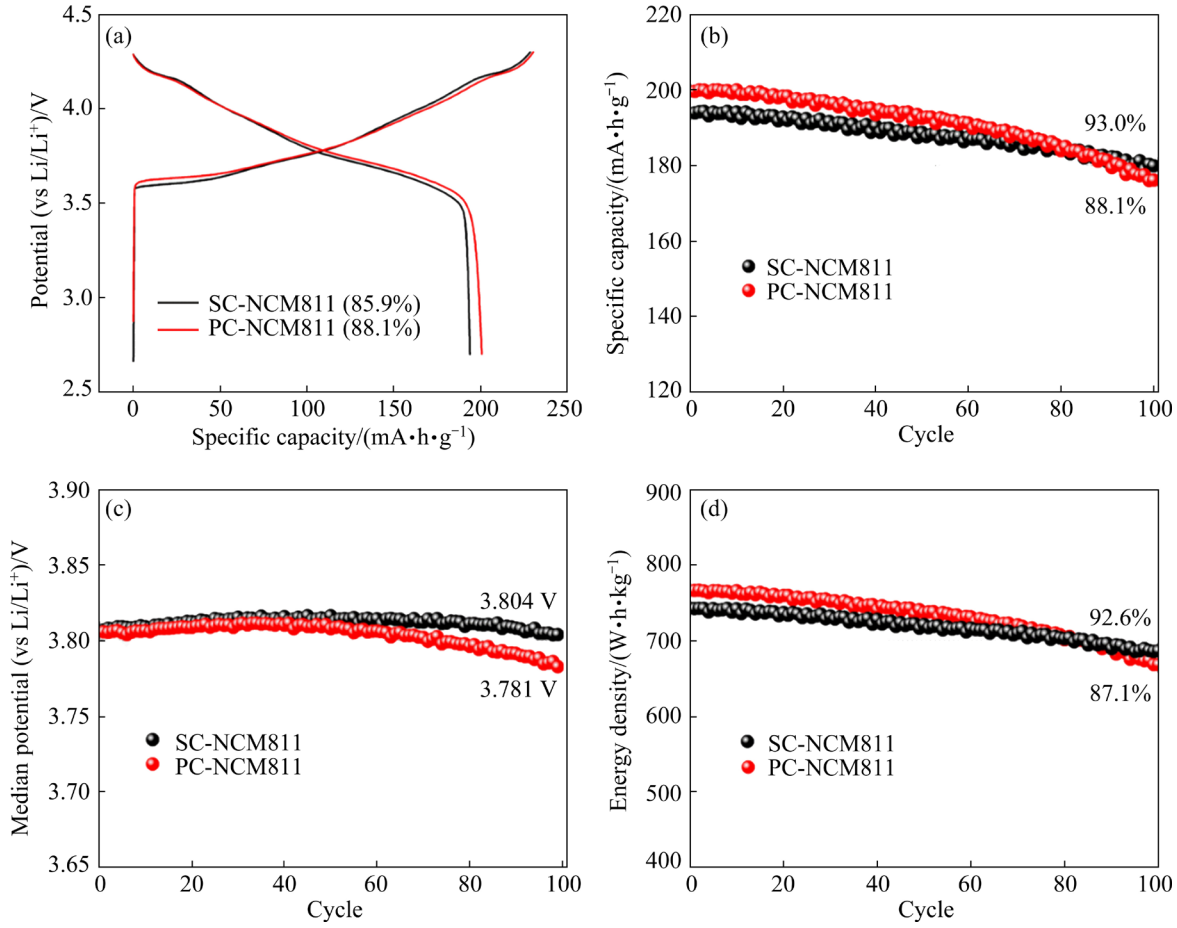

Fig. 6 Electrochemical properties of both NCM811 electrodes under upper cutoff of 4.3 V: (a) Initial cycling curves; (b−d) Cycling stabilities of capacity, median potential, and energy density at 0.1*C*, respectively

coulombic efficiency. Specifically, the SC-NCM811 electrode demonstrates a capacity retention of 93.0% after 100 cycles, while the PC-NCM811 retains 88.1% of its capacity. Furthermore, SC-NCM811 maintains a higher median potential of 3.804 V after 100 cycles, compared to 3.781 V for PC-NCM811. This improved stability in reversible capacity and median potential contributes to the superior stability of energy density in SC-NCM811. Changes in charge/discharge curves for both NCM811 electrodes from the 2nd to the 100th cycle are depicted in Fig. S4 of SI. SC-NCM811 shows weak changes in cycling curves, confirming the mitigated polarization during repeated cycles. These results reveal that, compared with PC-NCM811, SC-NCM811 has enhanced cycling stability under the upper cutoff of 4.3 V.

The rate properties of both NCM811 electrodes are evaluated from 0.1*C* to 5*C* in Figs. 7(a, c). The SC-NCM811 electrode exhibited specific capacities of 193, 188, 177, 167, 143, 116, and 80 mA·h/g from 0.1*C*, 0.2*C*, 0.5*C*, 1*C*, 2*C*, and 3*C* to 5*C*, respectively. The PC-NCM811 sample has specific capacities of 200, 196, 189, 181, 165, 151 and 130 mA·h/g at the same rates. SC-NCM811 is confirmed to exhibit a decreased specific capacity, especially at high rates above 2*C*, suggesting a decreased rate capability. The charge/discharge profiles indicate the worsened electrochemical polarization of the SC-NCM811 electrode.

GITT is utilized to examine the Li^+ chemical diffusion coefficients (D_{Li+}) of both SC-NCM811 and PC-NCM811. Figures 7(b, d) illustrate their typical GITT profiles along with the calculated D_{Li+}. The potential versus time profiles are presented in Figs. S5(a, c) of SI. A linear correlation between $\tau^{1/2}$ and potential is established in Figs. S5(b, d) of SI, facilitating the calculation of D_{Li+} based on the Fick's law [30,31].

$$D_{Li^+}=\frac{4}{\pi\tau}\left(\frac{mV_M}{MA}\right)^2\left(\frac{\Delta\varphi_s}{\Delta\varphi_\tau}\right)^2$$

where τ is the relaxation time, m represents the mass of the NCM811 cathode, M signifies the molar mass of the NCN811 cathode, A denotes the electrode area, V_M is the Li^+ molar volume. $\Delta\varphi_s$ is

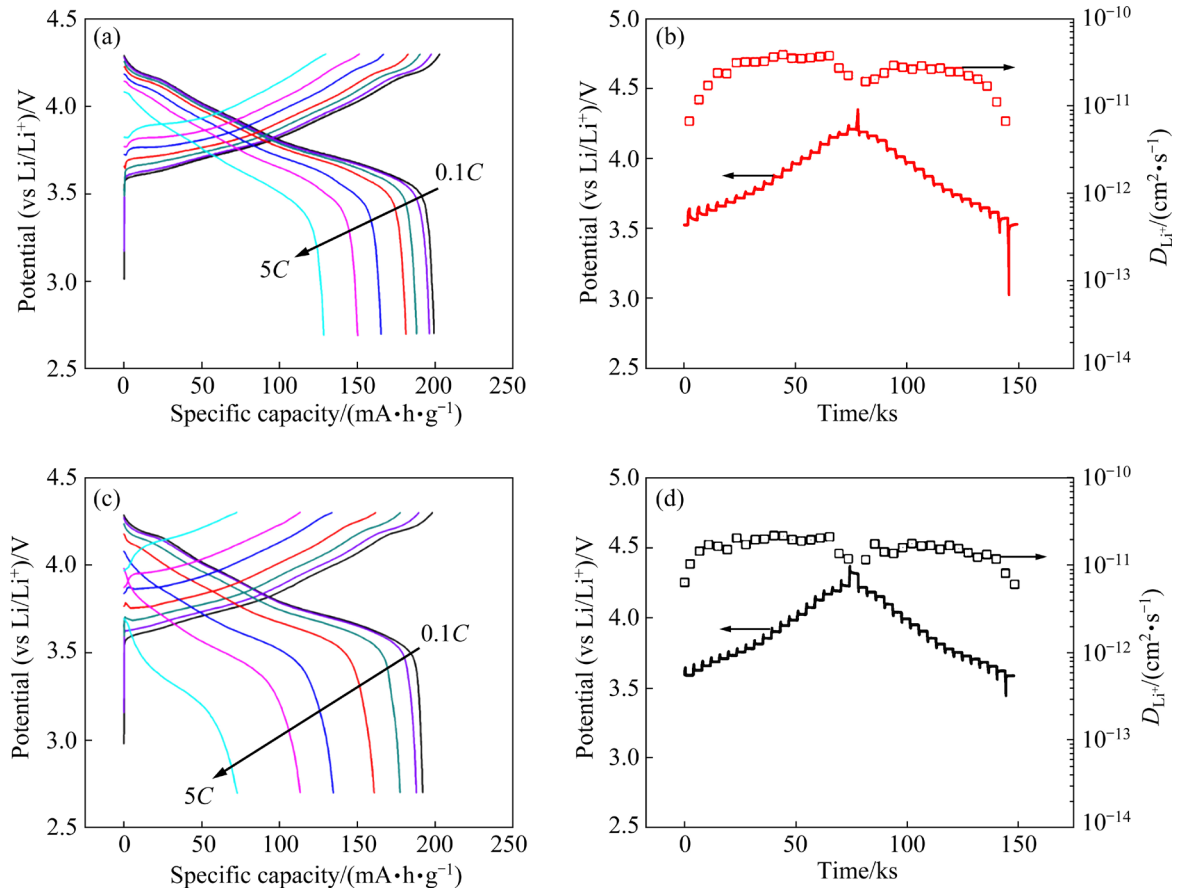

Fig. 7 Charge/discharge curves from 0.1*C* to 5*C* (a, c) and calculated Li^+ chemical diffusion coefficients (b, d): (a, b) PC-NCM811; (c, d) SC-NCM811

the total potential change caused by the pulse, and $\Delta\varphi_\tau$ is the potential change during constant current charge/discharge. For the PC-NCM811 electrode, D_{Li+} values range from 6.7×10^{-12} to 4.5×10^{-11} cm^2/s during charge/ discharge, with an average D_{Li+} value of 2.8×10^{-11} cm^2/s during charge and 2.3×10^{-11} cm^2/s during discharge. On the other hand, the SC-NCM811 sample exhibits D_{Li+} values ranging from 8.9×10^{-12} to 2.5×10^{-11} cm^2/s during charge/discharge, with an average D_{Li+} value of 1.9×10^{-11} cm^2/s during charge and 1.5×10^{-11} cm^2/s during discharge. These results indicate that the SC-NCM811 electrode possesses a lower average Li^+ chemical diffusion coefficient compared to its polycrystalline counterpart. This suggests that the single crystals, with an enlarged Li^+ diffusion path, lead to reduced redox kinetics and consequently hinder high-rate capability [32].

3.5 Thermal performance of SC- and PC-NCM811

The thermal stability of delithiated cathodes plays a crucial role in determining the safety of LIBs [33,34]. In highly charged Ni-rich cathodes, the release of lattice oxygen into the electrolyte can occur, potentially leading to thermal runaway and safety concerns in LIBs [24,35]. DSC is commonly used to assess the thermal stability of delithiated cathodes. The DSC curves for both delithiated NCM811 electrodes, charged to 4.3 V, are presented in Fig. 8. Both delithiated NCM811 samples exhibit a similar onset temperature of ~205 °C. However, the delithiated PC-NCM811 electrode displays a peak temperature of 223 °C, accompanied by a total heat release of 698.4 J/g. In contrast, the delithiated SC-NCM811 sample reveals two peak temperatures of 234 and 270 °C, with a total heat release of 506.2 J/g. The higher peak temperature and lower heat release during the thermal runaway of the delithiated SC-NCM811 electrode confirm its improved thermal stability.

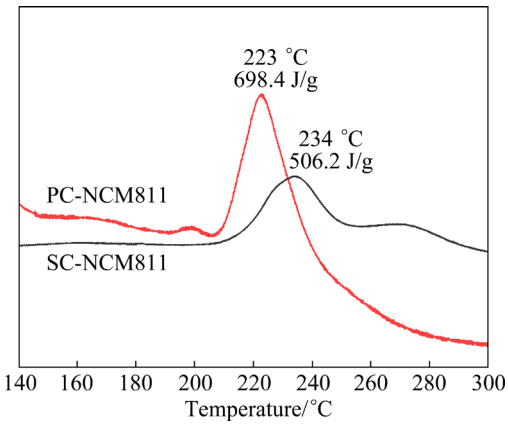

Fig. 8 DSC profiles of both delithiated NCM811 materials in fully charged state at 4.3 V

4 Conclusions

(1) The crystal growth rate and grain size of single-crystal NCM811 increase continuously as the heating rate rises from 2 to 8 °C/min. However, the higher heating rate of 8 °C/min exacerbates Li^+/Ni^{2+} cation mixing. A heating rate of 5 °C/min is preferable for the production of single-crystal Ni-rich cathodes with minimal cation mixing.

(2) Ab initio molecular dynamics simulations indicate that a high heating rate induces anabatic oscillations, suggesting a decrease in thermodynamic stability and a tendency for the crystal surface to undergo reconstruction. The intermediate phase at the grain boundary intensifies atomic migration-induced interface fusion, further enhancing crystal growth kinetics.

(3) Single-crystal NCM811 with a grain size of ~2 μm was prepared by optimizing the synthesis conditions. Compared with its polycrystalline counterpart, this material has an improved cycling lifespan and thermal stability but a decreased reversible capacity and high rate capability.

CRediT authorship contribution statement

Feng LI: Methodology, Writing − Review & editing, Funding acquisition; **Yu-hang TIAN:** Investigation, Formal analysis, Writing − Original draft; **Lu-xia GE** and **Sheng-long FAN:** Formal analysis; **Mao-sheng GONG:** Investigation, Formal analysis; **Ke FAN:** Investigation, Formal analysis, Writing − Review & editing; **Pei-yu HOU:** Conceptualization, Writing − Original draft, Funding acquisition; **Xian-qi WEI:** Formal analysis.

Declaration of competing interest

The authors declare that they have no known competing financial interests or personal relationships that could have appeared to influence the work reported in this paper.

Acknowledgments

This work was funded by the National Natural Science Foundation of China (No. 22379052), and

Taishan Scholars of Shandong Province, China (No. tsqnz20221143).

Supporting Information

Supporting Information in this paper can be found at: http://tnmsc.csu.edu.cn/download/16-p1975-2023-1070-Supporting_Information.pdf.

References

[1] TURCHENIUK K, BONDAREV D, SINGHAL V, YUSHIN G. Ten years left to redesign lithium-ion batteries [J]. Nature, 2018, 559: 467−470.

[2] CAO Yuan-lin, YANG Xiu-kang, WANG Lu, XIAO Ling, FU Ni, ZOU Li, MA Wen-bo, LIU Zhe-ting, WANG Xiao-qin, LIU Li, SHU Hong-bo, WANG Xian-you. Improving electrochemical performance of Ni-rich layered oxide cathodes via one-step dual modification strategy [J]. Transactions of Nonferrous Metals Society of China, 2022, 32: 3663−3678.

[3] GOODENOUGH J B, PARK K S. The Li-ion rechargeable battery: A perspective [J]. Journal of the American Chemical Society, 2013, 135: 1167−1176.

[4] LU Shi-jie, LIU Yang, HE Zhen-jiang, LI Yun-jiao, ZHENG Jun-chao, MAO Jing, DAI Ke-hua. Synthesis and properties of single-crystal Ni-rich cathode materials in Li-ion batteries [J]. Transactions of Nonferrous Metals Society of China, 2021, 31: 1074−1086.

[5] sNI Lian-shan, ZHANG Shu, DI An-di, DENG Wen-tao, ZOU Guo-qiang, HOU Hong-shuai, JI Xiao-bo. Challenges and strategies towards single-crystalline Ni-rich layered cathodes [J]. Advanced Energy Materials, 2022, 12: 2201510.

[6] LI Fang-cheng, ZHANG Gang, ZHANG Zong-liang, YANG Jian, LIU Fang-yang, JIA Ming, JIANG Liang-xing. Regeneration of Al-doped $LiNi_{0.5}Co_{0.2}Mn_{0.3}O_2$ cathode material by simulated hydrometallurgy leachate of spent lithium-ion batteries [J]. Transactions of Nonferrous Metals Society of China, 2022, 32: 593−603.

[7] WU Feng, LIU Na, CHEN Lai, SU Yue-feng, TAN Guo-qiang, BAO Li-ying, ZHANG Qi-yu, LU Yun, WANG Jing, CHEN Shi, TAN Jing. Improving the reversibility of the H2−H3 phase transitions for layered Ni-rich oxide cathode towards retarded structural transition and enhanced cycle stability [J]. Nano Energy, 2019, 59: 50−57.

[8] LIAN Meng-chen, SUN Qiang-chao, Wei, LIU Yan-bo, DUAN Tong, CHENG Hong-wei, LU Xiong-gang. Na^+-doped layered $LiNi_{1/3}Co_{1/3}Mn_{1/3}O_2$ cathode derived from low nickel matte with high structural stability and fast diffusion kinetics [J]. Transactions of Nonferrous Metals Society of China, 2023, 33: 3100−3112.

[9] SU Yue-feng, ZHANG Qi-yu, CHEN Lai, BAO Li-ying, LU Yun, CHEN Shi, WU Feng. Stress accumulation in Ni-rich layered oxide cathodes: Origin, impact, and resolution [J]. Journal of Energy Chemistry, 2022, 65: 236−253.

[10] HAN Dao-yuan, WENG Jing-zheng, ZHANG Xian, TONG Qing-song, ZHU Meng-qi. Review — Revealing the intercrystalline cracking mechanism of NCM and some regulating strategies [J]. Journal of the Electrochemical Society, 2022, 169: 040512.

[11] HOU Pei-yu, LIN Ze-zhou, LI Feng, XU Xi-jin. General synthesis of single-crystal spinel cathodes with the tailored orientation of exposed crystal planes for advanced lithium-ion batteries [J]. Small, 2023, 19: 2304482.

[12] QIU Lang, ZHANG Meng-ke, SONG Yang, XIAO Yao, WU Zheng-guo, XIANG Wei, LIU Yu-xia, WANG Gong-ke, SUN Yan, ZHANG Jun, ZHANG Bin, GUO Xiao-dong. Recent advance in structure regulation of high-capacity Ni-rich layered oxide cathodes [J]. EcoMat, 2021, 3: e12141.

[13] FAN Xin-ming, HU Guo-rong, ZHANG Bao, OU Xing, ZHANG Jia-feng, ZHAO Wen-gao, JIA Hai-ping, ZOU Lian-feng, LI Peng, YANG Yong. Crack-free single-crystalline Ni-rich layered NCM cathode enable superior cycling performance of lithium-ion batteries [J]. Nano Energy, 2020, 70: 104450.

[14] BI Yu-jing, TAO Jin-hui, WU Yu-qin, LI Lin-ze, XU Yao-bin, HU En-yuan, WU Bing-bin, HU Jiang-tao, WANG Chong-ming, ZHANG Ji-guang, QI Yue, XIAO Jie. Reversible planar gliding and microcracking in a single-crystalline Ni-rich cathode [J]. Science, 2020, 370: 1313−1317.

[15] ZHU He, TANG Yu, WIADEREK K M, BORKIEWICZ O J, REN Yang, ZHANG Jian, REN Jin-can, FAN Long-long, LI Cheng-chao, LI Dan-feng, WANG Xun-li, LIU Qi. Spontaneous strain buffer enables superior cycling stability in single-crystal nickel-rich NCM cathode [J]. Nano Letters, 2021, 21: 9997−10005.

[16] LIANG Wen-biao, JIN Feng, ZHAO Yin, SHI Li-yi, LIU Quan, WANG Zhu-yi, WANG Yi, ZHANG Mei-hong, ZHU Jie-fang, YUAN Shuai. Synthesis of single-crystal $LiNi_{0.8}Co_{0.1}Mn_{0.1}O_2$ materials for Li-ion batteries by microfluidic technology [J]. Chemical Engineering Journal, 2023, 464: 142656.

[17] TAKAMORI S, DOI T, INABA M. Aluminum doping effects on large $LiNi_{0.8}Co_{0.1}Mn_{0.1}O_2$ single crystal particles prepared in a molten $LiOH−Li_2SO_4$ flux [J]. Journal of the Electrochemical Society, 2023, 170: 020532.

[18] LANGDON J, MANTHIRAM A. A perspective on single-crystal layered oxide cathodes for lithium-ion batteries [J]. Energy Storage Materials, 2021, 37: 143−160.

[19] LIU Jing-jie, YUAN Yi-fei, ZHENG Jian-hui, WANG Li-guang, JI Jie, ZHANG Qing, YANG Lin, BAI Zheng-yu, LU Jun. Understanding the synthesis kinetics of single-crystal Co-free Ni-rich cathodes [J]. Angewandte Chemie-International Edition, 2023, 62: e202302547.

[20] ZHAO Jian-qing, ZHANG Wei, HUQ A, MISTURE S T, ZHANG Bo-liang, GUO Sheng-min, WU Li-jun, ZHU Yi-mei, CHEN Zong-hai, AMINE K, PAN Feng, BAI Jian-ming, WANG Feng. In situ probing and synthetic control of cationic ordering in Ni-rich layered oxide cathodes [J]. Advanced Energy Materials, 2017, 7: 1601266.

[21] LI Jing, LI Hong-yang, STONE W, WEBER R, HY S, DAHN J R. Synthesis of single crystal $LiNi_{0.5}Mn_{0.3}Co_{0.2}O_2$ for lithium ion batteries [J]. Journal of the Electrochemical Society, 2017, 164: A3529−A3537.

[22] QIU Lang, ZHANG Meng-ke, SONG Yang, WU Zhen-guo, ZHANG Heng, HUA Wei-bo, SUN Yan, KONG Qing-quan,

FENG Wei, WANG Ke, XIAO Yao, GUO Xiao-dong. Origin and regulation of interface fusion during synthesis of single-crystal Ni-rich cathodes [J]. Angewandte Chemie-International Edition, 2023, 62: e202300209.

[23] ZHANG Hong-wei, CEN Tian, TIAN Yan-hong, ZHANG Xue-jun. Synthesis of high-performance single-crystal $LiNi_{0.8}Co_{0.1}Mn_{0.1}O_2$ cathode materials by controlling solution super-saturation [J]. Journal of Power Sources, 2022, 532: 231037.

[24] SHEN Ji-xue, ZHANG Bao, HUANG Wei-yuan, LI Xiao, XIAO Zhi-ming, WANG Jing, ZHOU Tao, WEN Jiang-guo, LIU Tong-chao, AMINE K, OU Xing. Achieving thermodynamic stability of single-crystal Co-free Ni-rich cathode material for high voltage lithium-ion batteries [J]. Advanced Functional Materials, 2023, 33: 2300081.

[25] FAN Xin-ming, OU Xing, ZHAO Wen-gao, LIU Yun, ZHANG Bao, ZHANG Jia-feng, ZOU Lian-feng, SEIDL L, LI Yang-zhong, HU Guo-rong, BATTAGLIA C, YANG Yong. In situ inorganic conductive network formation in high-voltage single-crystal Ni-rich cathodes [J]. Nature Communications, 2021, 12: 5320.

[26] ZHOU Fu, ZHAO Xue-mei, VAN BOMMEL A, ROWE A W, DAHN J R. Coprecipitation synthesis of $Ni_xMn_{1-x}(OH)_2$ mixed hydroxides [J]. Chemistry of Materials, 2010, 22: 1015−1021.

[27] QIU Lang, ZHANG Meng-ke, SONG Yang, WU Zhen-guo, HU Kang-hui, YUE Lu-chao, ZHANG Jun, MING Yong, XIANG Wei, WANG Gong-ke, LIU Yu-xia, SUN Yan, GUO Xiao-dong. The structure-activity relationship between precursor fine structure and cathode performance in ultra-high Ni layered oxide [J]. Chemical Engineering Science, 2022, 260: 117865.

[28] HOU Pei-yu, LI Feng, SUN Yan-yun, PAN Mei-ling, WANG Xiao, SHAO Ming-hui, XU Xi-jin. Improving Li^+ kinetics and structural stability of nickel-rich layered cathodes by heterogeneous inactive-Al^{3+} doping [J]. ACS Sustainable Chemistry & Engineering, 2018, 6: 5653−5661.

[29] MENG Y S, CEDER G, GREY C P, YOON W S, YANG S H. Understanding the crystal structure of layered $LiNi_{0.5}Mn_{0.5}O_2$ by electron diffraction and powder diffraction simulation [J]. Electrochemical and Solid-state Letters, 2004, 7: A155.

[30] FENG Yan, CAO Cai-yu, ZENG Jing, WANG Ri-chu, PENG Chao-qun, WANG Xiao-feng. Hierarchical porous Co_3O_4 spheres fabricated by modified solvothermal method as anode material in Li-ion batteries [J]. Transactions of Nonferrous Metals Society of China, 2022, 32: 1253−1260.

[31] LI Feng, FAN Ke, HOU Pei-yu, HUANG Hai-tao. Boosting the redox kinetics of high-voltage P2-type cathode by radially oriented {010} exposed nanoplates for high-power sodium-ion batteries [J]. Small Structures, 2022, 3: 2100123.

[32] DENG Xian-ming, ZHANG Rui, ZHOU Kai, GAO Zi-yao, HE Wei, ZHANG Li-han, HAN Cui-ping, KANG Fei-yu, LI Bao-hua. A comparative investigation of single crystal and polycrystalline Ni-rich NCMs as cathodes for lithium-ion batteries [J]. Energy & Environmental Materials, 2023, 6: e12331.

[33] HUANG Yu-zhu, XING Lin, PEI Shuang, ZHOU Wei, HU Yu-jie, DENG Wei-na, CHEN Liang, ZHU Hai, CHEN Han. Co_9S_8/CNTs microspheres as superior-performance cathodes in aqueous ammonium-ion batteries [J]. Transactions of Nonferrous Metals Society of China, 2023, 33: 3452−3464.

[34] FENG Xu-ning, REN Dong-sheng, HE Xiang-ming, OUYANG Ming-gao. Mitigating thermal runaway of lithium-ion batteries [J]. Joule, 2020, 4: 743−770.

[35] WANG Chun-yang, HAN Li-li, ZHANG Rui, CHENG Hao, MU Lin-qin, KISSLINGER K, ZOU Pei-chao, REN Yang, CAO Peng-hui, LIN Feng, XIN Huo-lin. Resolving atomic-scale phase transformation and oxygen loss mechanism in ultrahigh-nickel layered cathodes for cobalt-free lithium-ion batteries [J]. Matter, 2021, 4: 2013−2026.

高比能锂离子电池单晶高镍层状正极材料的晶体生长动力学

李 凤[1]，田宇航[1]，葛露霞[1]，樊盛龙[1]，公茂盛[1]，范 稞[2]，侯配玉[1]，魏显起[1]

1. 济南大学 物理科学与技术学院，济南 250022；
2. 香港理工大学 应用物理系 智能能源研究院，香港 999077

摘 要：系统地研究合成条件，尤其是升温速率对高镍正极反应动力学的影响规律。研究发现，随着升温速率的升高，高镍氧化物的生长速率随之升高。从头算分子动力学模拟表明：高升温速率引起平衡位置急剧震荡，降低了体系热力学稳定性，导致晶体表面倾向发生结构重构。晶界中间相形成有助于加快原子扩散诱导的界面融合，提高晶体生长动力学。然而，过快的升温速率会加剧高镍正极材料 Li^+/Ni^{2+}混排。相比于多晶体，单晶高镍正极具有改善的结构和热稳定性，但是降低了比容量和倍率性能。

关键词：锂离子电池；高镍正极；单晶；生长动力学；升温速率

(Edited by Xiang-qun LI)